Electrochemical and Solid-State Letters, **10** (12) B214-B217 (2007)
1099-0062/2007/10(12)/B214/4/$20.00 © The Electrochemical Society

Three-Dimensional Reconstruction of Porous LSCF Cathodes

D. Gostovic,*,z J. R. Smith,* D. P. Kundinger, K. S. Jones, and E. D. Wachsman****

University of Florida–U.S. Department of Energy High Temperature Electrochemistry Center, University of Florida, Gainesville, Florida 32611-6400, USA

In this initial study the electrochemically active region of a $La_{0.8}Sr_{0.2}Co_{0.2}Fe_{0.8}O_{3-\delta}$ (LSCF) cathode was reconstructed in three dimensions using a focused ion beam/scanning electron microscope. The reconstructed volume totaled 1065 μm^3 from the free air surface to the dense yttria-stabilized zirconia electrolyte interface. Various microstructural properties were measured, including overall porosity, closed porosity, graded porosity, surface area, tortuosity, triple-phase boundary length, and pore size. Electrochemical impedance spectroscopy data was correlated to microstructure.
 [DOI: 10.1149/1.2794672]

Manuscript submitted October 31, 2006; revised manuscript received September 10, 2007.
Available electronically October 15, 2007.

Solid oxide fuel cells (SOFCs) are efficient, environmentally friendly, and fuel-flexible electrochemical devices for the generation of electrical power and heat.[1] They consist of three basic layers: cathode, electrolyte, and anode. The cathode is a porous, conductive catalyst for the reduction of O_2 and for the oxidation of fuel. Between the cathode and anode is the dense electrolyte. The circuit is completed via cathode and anode contacts to an external load.

The basic chemical formula for the cathodic reduction reaction is

$$\frac{1}{2}\,O_2 + V_o^{\cdot\cdot} + 2e' = O_o^x \qquad [1]$$

Current SOFC performance is limited by cathode polarization, which increases with decreasing operational temperatures.[2,3] Cathode microstructure and morphology have a strong effect on this polarization.[2-4] In this initial study a dual-beam focused ion beam/scanning electron microscope (FIB/SEM) was utilized to reconstruct an actual three-dimensional (3D) model of a $La_{0.8}Sr_{0.2}Co_{0.2}Fe_{0.8}O_{3-\delta}$ (LSCF) cathode and its interface with a dense yttrium-stabilized zirconia (YSZ) electrolyte. This high-resolution, 3D technique advances the understanding of the cathode microstructure's effect on performance. The identification of critical microstructural properties such as surface area, tortuosity, and interfacial porosity may be correlated with the ionic, electronic, and catalytic processes for a better fundamental understanding of electrochemical performance. With this tool, SOFC material and microstructural design can be more effective in reducing cathodic polarization at lower operational temperatures.

The semiconductor industry has used the FIB since the 1980s to deposit, etch, micromachine, and image specimens during different stages of circuit processing.[5,6] This technology was brought forward to reconstruct 3D, geometrically complex submicrometer structures.[7-11] With the advent of 3D modeling software, nanotomography utilizing the dual-beam FIB/SEM technique was used to quantify nanoceramic suspended powders.[10-12] This technique was applied to SOFC cermet anodes to quantify microstructural properties such as porosity, triple-phase-boundary (TPB) length, and degree of anisotropy via tortuosity.[13] Such a technique has never before been applied to reconstruct a cathode and the cathode/electrolyte interface.

Experimental

Square LSCF symmetric cell cathodes (8×8 mm) were screen printed using premixed LSCF ink (NexTech Materials, Inc.) on both sides of a 100 μm thick polycrystalline YSZ electrolyte (Marketech International, Inc.) using common techniques.[14] After low-temperature drying to eliminate the organic vehicle, three samples were sintered at 850, 950, and 1100°C, respectively, for 1 h. The resulting porous cathode films were approximately 20 μm thick. Impedance measurements were collected in air, with platinum mesh pressure contacts using a Solartron 1260 frequency-response analyzer under a potentiostatic modulation of 50 mV. The frequency range was 10 MHz to 10 mHz with ten points per decade.

The automated sectioning and imaging was conducted with a FEI Strata DB 235 FIB/SEM dual-beam system. A schematic of the dual-beam orientation is shown in Fig. 1. The ion and electron pole pieces are oriented at 52°. The system has an in situ liquid

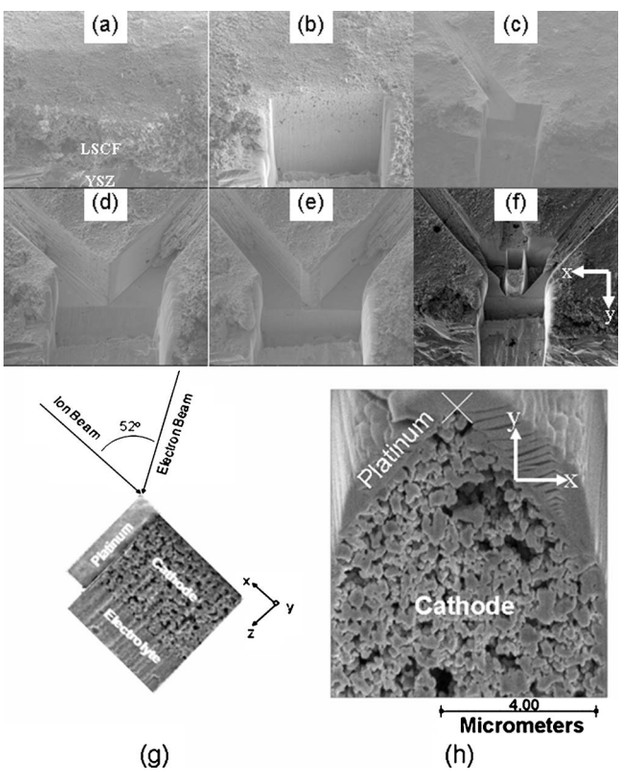

Figure 1. (a) As-cracked LSCF/YSZ sample cross section; (b) front milling with FIB; (c, d) angled milling to create fiduciary mark in *x*-*y* plane; (e) platinum deposition to protect fiduciary mark; (f) zero tilt view of area to be milled/reconstructed, *z* axis points into plane of page; (g) schematic of ion and electron beams incident upon ROI which consists of a platinum protection layer, porous cathode, and dense electrolyte; and (h) representative FEG-SEM image of actual reconstructed LSCF cathode with platinum protection layer, and fiduciary ridgeline present.

* Electrochemical Society Student Member.
** Electrochemical Society Active Member.
z E-mail: gostovic@ufl.edu

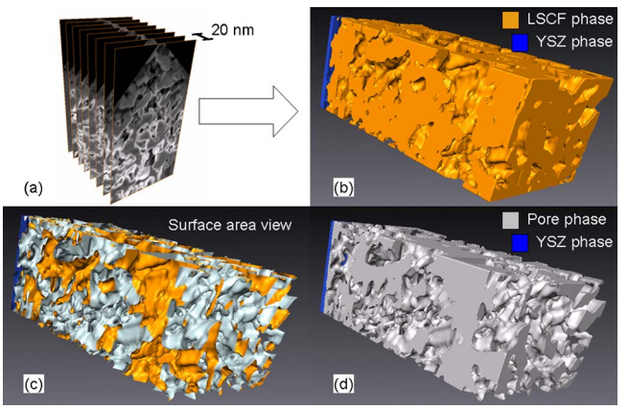

Figure 2. (Color online) (a) SEM two-dimensional images were stacked, aligned, and reconstructed into a (b) 3D triangular mesh representing actual LSCF/YSZ interfacial microstructure sintered at 950°C. This allows for measurement of (c) surface area and (d) volume porosity.

metallorganic ion source (LMIS) for the deposition of protective platinum layers. Rastering the FIB across the region of interest (ROI) physically sputters away material, which is redeposited locally. The field emission gun (FEG) SEM was utilized to image the freshly milled surface with a through-lens detector (TLD) down to a maximum lateral (x, y in Fig. 1) resolution of 3 nm. The TLD's charging contrast was used to distinguish between the electrolyte and cathode phases. This FIB method was used to create a trench around the ROI which is visible in Fig. 1. The ROI resembles a pillar, with a dense layer of platinum deposited on top to protect the microstructure while trenching. There are three advantages to using the pillar technique. First, redeposition or curtaining is not seen in the SEM images; thus, there is no obstruction. Second, the image brightness gradient is flatter, which aids in software-assisted segmentation. Third, the pillar geometry can be used to align the sample in the x-y plane with a single point at the top of the houselike cross section. The pillar was sliced in the z direction from the air/cathode surface toward the cathode/electrolyte interface (Fig. 1). The slicing resolution was 20 nm. This process of slicing and imaging was expedited with the Auto Slice and View software package (FEI Co.). Additionally, ion images were captured at regular intervals during the automated slicing, so as to corroborate the z direction slice thickness.

Results and Discussion

Amira-ResolveRT version 4.0 (Mercury Computer Systems, Inc.) was utilized to align, segment, and concatenate the serial images into a 3D triangular mesh (movie: http://hitec.mse.ufl.edu/, Fig. 2). Three pillars were reconstructed for each sintering condition. The total reconstructed volumes were 399, 227, and 439 μm^3 for the 850, 950, and 1100°C temperatures, respectively (Table I). The

Table I. Summary of microstructural properties measured from 3D reconstructions of LSCF sintered at various temperatures for 1 h.

	Sintering temperature (°C)		
	850	950	1100
Total reconstructed volume (μm^3)	399.4	227.2	438.7
Porosity (vol %)	21.7 ± 2.6	25.2 ± 12.8	32.4 ± 4.7
Surface area/volume (μm^{-1})	9.3 ± 1.1	8.8 ± 0.8	7.2 ± .04
Average pore diameter (nm)	140.9 ± 17.0	173.6 ± 94.7	268 ± 24.4
Tortuosity	2.5 ± 0.4	2.6 ± 0.5	2.8 ± 1.0
TPB length/area (μm^{-1})	3.2 ± 1.6	4.1 ± 2.5	2.5 ± 0.1

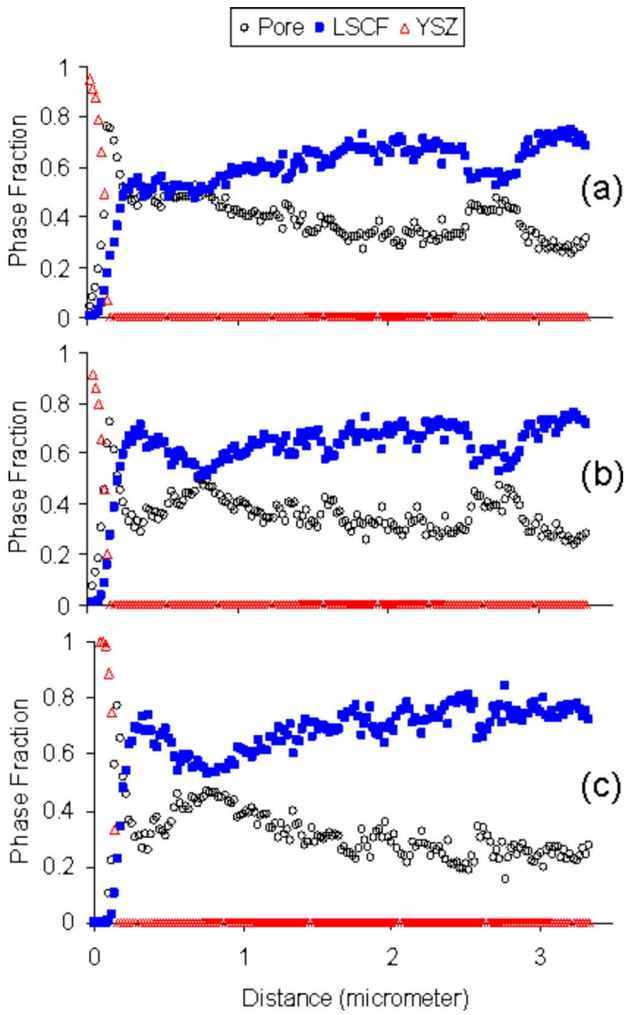

Figure 3. (Color online) Graded phase fraction plot of various phases close to the LSCF/YSZ interface (sintered at 950°C) of (a) quadruple-volume, (b) double-volume, and (c) single-volume reconstructions. The x axis is distanced away from the electrolyte. The y axis is the phase fraction of each phase.

Amira tissue statistics module was used to calculate the volume pore fraction. The volume porosity was 21.7 ± 2.6, 25.2 ± 12.8, and 32.4 ± 4.7% for the 850, 950, and 1100°C temperatures, respectively. The high standard deviation in the 950°C sample is attributed to selective sampling. The second and third ROIs were chosen to eliminate the large pores observed in the initial reconstruction. The increasing trend in porosity with sintering temperature is attributable to resolution, as all nine samples were imaged at identical magnification levels. The resolution limit influences the small pore/particle size of the 850°C sample more than the coarser 950 and 1100°C samples. When the 950°C data was resampled by a 2:1 ratio (the equivalent of imaging at half the original magnification) a 6% reduction in the porosity was observed. This exemplifies the influence of resolution on reconstruction statistics. Similar resampling porosity variation was seen in a previous NiO-YSZ anode FIB/SEM 3D study.[13] The closed porosity was negligible for all nine reconstructions. To eliminate edge effects closed porosity was measured after cropping the reconstruction's outer edges by 5 vol %, but no change in closed porosity was observed.

Graded porosity was plotted to gauge the uniformity of phases through the first 950°C reconstructed volume (Fig. 3). A common feature regardless of volume size or sintering temperature is high

porosity at the LSCF/YSZ interface (~50%), indicating that the cathode is not very well sintered to the YSZ. Using a small volume size inaccurately suggests a fine bulk pore structure. For the 950°C sample seen in Fig. 2, the volume porosity is 31.9% with a smooth graded porosity profile indicative of uniform pore/grain size (Fig. 3c). Increasing sample size leads to the appearance of larger pores in the volume and subsequent increases in porosity. Doubling the sample volume yields a 36.6% porosity and a large pore appears around 2.75 μm on the graded porosity profile (Fig. 3b). Quadrupling the volume further increases the porosity to 39.9% with the roughest graded porosity profile (Fig. 3a). The large pore centered at 2.75 μm is still present, and another large pore appears between the interface and 0.8 μm. The increasing roughness of the graded porosity profiles seen with increasing sample size was also observed with increasing sintering temperature. The 850°C reconstructions generally had smoother profiles than the coarser 1100°C reconstructions. This elucidates the importance of optimizing sample size and resolution in order to yield representative data.

An Amira tissue statistics module allowed for measurement of the surface area between the cathode and open pores (Fig. 2c, Table I). Sintering temperatures of 850, 950, and 1100°C correspond to volume-normalized surface areas of 9.3 ± 1.1, 8.8 ± 0.8, and 7.2 ± 0.4 μm^{-1}, respectively. This trend indicates that the measured surface area is decreasing due to pore coarsening. These surface area values are 3–4 times higher than the comparably measured pore surface area of a coarser-grained SOFC composite anode (2.4 μm^{-1}).[13] Another indication of microstructural coarsening is the TPB length per area. The TPB lengths were measured as 3.2 ± 1.6, 4.1 ± 2.5, and 2.5 ± 0.1 μm^{-1} for the sintering temperatures of 850, 950, and 1100°C (Table I). These values are higher than comparably fired LSM cathodes of ~1 μm^{-1} [15] and follow the same trend observed in other cathodes fired on YSZ,[16] with a maximum in TPB length occurring for the optimally sintered cathode (950°C).

A common technique for particle/pore size calculations is the use of the Brunauer–Emmett–Teller (BET) formula $d = 6$ V/S.[10,17] Using the volume, surface area, and porosity, the pore diameters were measured as 140.9 ± 17, 173.6 ± 94.7, and 268.9 ± 24.4 nm for the 850, 950, and 1100°C sintering temperatures, respectively. The high variation in the 950°C sample is attributable to previously mentioned sampling issues. This increase in pore size is inversely proportional to the surface area when using the BET method.[17]

Tortuosity was measured using Amira's center of mass calculations. Tortuosity was quantified by tracking the center of mass of each pore as it goes from the surface of the cathode to the YSZ interface. The total length of this path was divided by the Euclidian distance between the air/cathode interface and cathode/electrolyte interface. The measured tortuosities for the 850, 950, and 1100°C sintering temperatures were 2.5 ± 0.4, 2.6 ± 0.5, and 2.8 ± 1.0, respectively. This is within the range of 1.5–7.8 previously published for various porous cathodes with ~30% porosity.[18,19] The increasing tortuosity is caused by pore coarsening.[20-23] Coarsening causes higher standard deviation in tortuosity caused by the variance in the pore size distribution.

Prior to serial sectioning, electrochemical impedance spectrometry (EIS) was performed on all three symmetric cathode samples at various temperatures and oxygen partial pressures. Typical scan results collected at 700°C in air are shown in Fig. 4 and Table II. The total (nonohmic) cathode polarization increases with sintering temperature. The 1100°C sintered sample has a cathodic polarization of 101.89 Ω cm^2, which is two orders of magnitude higher than the 850 and 950°C cathodic polarizations of 0.65 and 0.87 Ω cm^2, respectively. Despite this, the 1100°C sample's total ohmic polarization of 2.11 Ω cm^2 is less than that of the 850 and 950°C samples (Table I), indicative of better sintering at the YSZ/LSCF interface. The relationship between cathodic polarization and various microstructural properties is shown in Fig. 5. The trends indicate that one reason for increases in cathodic polarization is decreasing surface area due to coarsening of the microstructure with sintering.

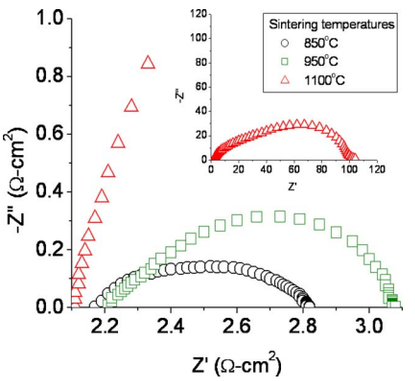

Figure 4. (Color online) EIS spectra of LSCF collected at 700°C in air. The inset displays the 1100°C sintering temperature scan.

Table II. Summary of EIS data for symmetric LSCF cathode collected at 700 °C in air.

	Sintering temperature (°C)		
	850	950	1100
Cathodic polarization (Ω cm^2)	0.65	0.87	101.89
Ohmic polarization (Ω cm^2)	2.17	2.21	2.11
Peak frequency (Hz)	90	316	1

The volume fraction of porosity, V_V, divided by the tortuosity, τ, is related to the effective diffusion coefficient, $D_{\text{cath (eff)}}$ [24]

$$D_{\text{cath (eff)}} = D_{\text{cath}} V_v/\tau \quad [2]$$

Thus, a reduction in V_v/τ would decrease the effective O_2 diffusion through the cathode, resulting in an increase in any cathodic polarization attributable to gas diffusion. As seen in Fig. 5, the plot of cathodic polarization vs V_V/τ indicates that these microstructural features play a role in the cathodic polarization. Additionally, the increases in cathodic polarization may be due to decreasing TPB length (Table I) and the appearance of interfacial tertiary phases at high sintering temperatures.[25-27] Ongoing work will solidify the LSCF microstructure-performance relationship, both with additional

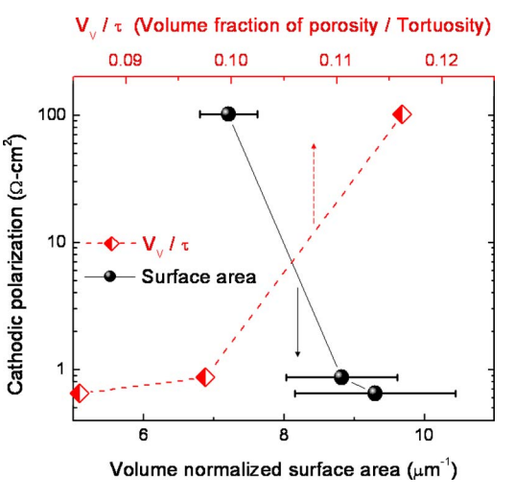

Figure 5. (Color online) Cathodic polarization (collected at 700°C in air) plotted vs V_V/τ (top *x* axis), and surface area (bottom *x* axis).

sample reconstructions and impedance analysis, as a function of temperature and p_{O_2}.

Conclusion

In this initial study we successfully reconstructed a 3D model of an actual LSCF cathode. This provides the ability to quantify porous cathode microstructures at the submicrometer level. This technique allows researchers to quantify microstructural properties in between processing steps and at specific sites. Further, this technique has allowed us to develop the direct link between the microstructure and performance relationship in SOFC cathodes.[28,15]

Acknowledgments

The authors thank the University of Florida–U.S. Department of Energy High Temperature Electrochemistry Center for funding the project (DE-AC05-76RL01830); the Major Analytical Instrumentation Center, Department of Materials Science and Engineering, University of Florida, for the use of its facilities; and NexTech Materials for the inks and powders used in the study. Additionally, we thank Lorenz Holzer, Jerry Bourne, Keith Duncan, and Aijie Chen for their insightful discussions.

The University of Florida assisted in meeting the publication costs of this article.

References

1. N. Q. Minh, *J. Am. Ceram. Soc.*, **76**, 563 (1993).
2. F. Zhao, Y. Jiang, G. Y. Lin, and A. V. Virkar, in *Solid Oxide Fuel Cells VII*, H. Yokokawa and S. C. Singhal, Editors, PV 2001-16, p. 501, The Electrochemical Society Proceedings Series, Pennington, NJ (2001).
3. S. B. Adler, *Chem. Rev.*, **104**, 4791 (2004).
4. J. H. Lee, H. Moon, H. W. Lee, J. Kim, J. D. Kim, and K. H. Yoon, *Solid State Ionics*, **148**, 15 (2002).
5. E. C. G. Kirk, R. A. McMahon, J. R. A. Cleaver, and H. Ahmed, *J. Vac. Sci. Technol. B*, **6**, 1940 (1988).
6. J. Orloff, *Rev. Sci. Instrum.*, **64**, 1105 (1993).
7. D. N. Dunn and R. Hull, *Appl. Phys. Lett.*, **75**, 3414 (1999).
8. D. N. Dunn, G. J. Shiflet, and R. Hull, *Rev. Sci. Instrum.*, **73**, 330 (2002).
9. R. K. Bansal, A. Kubis, R. Hull, and J. M. Fitz-Gerald, *J. Vac. Sci. Technol. B*, **24**, 554 (2006).
10. L. Holzer, F. Indutnyi, P. H. Gasser, B. Munch, and M. Wegmann, *J. Microsc.*, **216**, 84 (2004).
11. L. Holzer, B. Muench, M. Wegmann, P. Gasser, and R. J. Flatt, *J. Am. Ceram. Soc.*, **89**, 2577 (2006).
12. B. Munch, P. Gasser, L. Holzer, and R. Flatt, *J. Am. Ceram. Soc.*, **89**, 2586 (2006).
13. J. R. Wilson, W. Kobsiriphat, R. Mendoza, H. Y. Chen, J. M. Hiller, D. J. Miller, K. Thornton, P. W. Voorhees, S. B. Adler, and S. A. Barnett, *Nat. Mater.*, **5**, 541 (2006).
14. J. R. Smith, M. E. Orazem, K. Duncan, A. Chen, and E. D. Wachsman, *ECS Trans.*, **1**(7), 243 (2006).
15. J. R. Smith, A. Chen, D. Gostovic, D. Hickey, D. P. Kundinger, K. L. Duncan, R. T. DeHoff, K. S. Jones, and E. D. Wachsman, *Solid State Ionics*, Submitted.
16. J. Mizusaki, H. Tagawa, K. Tsuneyoshi, and A. Sawata, *J. Electrochem. Soc.*, **138**, 1867 (1991).
17. S. Brunauer, P. H. Emmett, and E. Teller, *J. Am. Chem. Soc.*, **60**, 309 (1938).
18. B. C. H. Steele, *Solid State Ionics*, **134**, 3 (2000).
19. F. Zhao, T. J. Armstrong, and A. V. Virkar, *J. Electrochem. Soc.*, **150**, A249 (2003).
20. P. Wong, J. Koplik, and J. P. Tomanic, *Phys. Rev. B*, **30**, 6606 (1984).
21. A. S. Wagh, R. B. Poeppel, and J. P. Singh, *J. Mater. Sci.*, **26**, 3862 (1991).
22. K. L. Duncan, J. F. Lodenquai, A. S. Wagh, and K. C. Goretta, *J. Appl. Phys.*, **84**, 2665 (1998).
23. Y. S. Wu, L. J. van Vliet, H. W. Frijlink, and K. V. D. Maarschalk, *Eur. J. Pharm. Sci.*, **28**, 433 (2006).
24. J. W. Kim, A. V. Virkar, K. Z. Fung, K. Mehta, and S. C. Singhal, *J. Electrochem. Soc.*, **146**, 69 (1999).
25. M. Kleitz and F. Petitbon, *Solid State Ionics*, **92**, 65 (1996).
26. H. Y. Lee and S. M. Oh, *Solid State Ionics*, **90**, 133 (1996).
27. H. Y. Tu, Y. Takeda, N. Imanishi, and O. Yamamoto, *Solid State Ionics*, **100**, 283 (1997).
28. E. D. Wachsman, *Fundamental Mechanisms of SOFC Cathode Reactions*, 2006 (available from http://www.netl.doe.gov/publications/proceedings/06/seca/pdf/Wachsman.pdf).